coatings

MDPI

Article

Self-Healing and Thermal Stability of $LaMgAl_{11}O_{19}$-Ti_3AlC_2 Composites for High-Temperature Abradable Applications

Jingqi Huang, Wenbo Chen, Kaiyue Lü, Mingyi Xu, Longhui Deng, Jianing Jiang, Shujuan Dong, Meizhu Chen * and Xueqiang Cao *

State Key Laboratory of Silicate Materials for Architectures, Wuhan University of Technology, Wuhan 430070, China

* Correspondence: chenmzh@whut.edu.cn (M.C.); xcao@whut.edu.cn (X.C.)

Abstract: Defects such as interconnected pores and cracks can improve the abradability of ceramic-based abradable sealing coatings (ASCs) but may reduce the lifetime. Self-healing can potentially close cracks and transform interconnected pores into isolated ones through filling and sintering effects. Ti_3AlC_2 (TAC) was incorporated into $LaMgAl_{11}O_{19}$ (LMA) as both the self-healing agent and sintering aid, and plasma-sprayed LMA-based composite coatings were annealed at 1200 °C to assess their self-healing capabilities and then subjected to oxidation in air and corrosion in steam at 1300 °C to study their long-term stability. Results indicated that increasing TAC content significantly enhances self-healing effectiveness, evidenced by the closure of cracks and the isolation of pores. Oxidation and corrosion at 1300 °C led to significant grain growth and the formation of equiaxed grains with an aspect ratio of approximately 3, which may impair the toughening mechanism. Meanwhile, due to the preferential volatilization of Al in a steam environment, LTA decomposed into α-$La_{2/3}TiO_3$ and $La_4Ti_3O_{12}$ phases, and the accelerated mass transfer also resulted in grain coarsening. Interestingly, the L20T composite coating with a porosity of 32.17 ± 0.94% and a hardness of 74.88 ± 1.55 HR15Y showed great potential for abradable applications due to its stable phase composition and uniform pore distribution.

Keywords: $LaMgAl_{11}O_{19}$; Ti_3AlC_2; abradable sealing coatings; self-healing; sintering

check for updates

Citation: Huang, J.; Chen, W.; Lü, K.; Xu, M.; Deng, L.; Jiang, J.; Dong, S.; Chen, M.; Cao, X. Self-Healing and Thermal Stability of $LaMgAl_{11}O_{19}$-Ti_3AlC_2 Composites for High-Temperature Abradable Applications. *Coatings* **2024**, *14*, 938. https://doi.org/10.3390/coatings14080938

Academic Editors: Kamalan Kirubaharan Amirtharaj Mosas and Omid Sharifahmadian

Received: 2 July 2024
Revised: 21 July 2024
Accepted: 24 July 2024
Published: 26 July 2024

Copyright: © 2024 by the authors. Licensee MDPI, Basel, Switzerland. This article is an open access article distributed under the terms and conditions of the Creative Commons Attribution (CC BY) license (https://creativecommons.org/licenses/by/4.0/).

1. Introduction

Abradable sealing coatings (ASCs) are applied to the inner walls of aero-engine casings, where they rub against the rotor blades. This process aims to minimize gas path clearances through the preferential wear of the ASCs, thereby enhancing efficiency, reducing emissions, and preventing unexpected damage caused by severe rotor–stator contact [1]. For turbine seals, ceramic materials with higher melting points are typically used as the abradable matrixes. Among them, yttria-stabilized zirconia (YSZ) material, widely studied in the thermal barrier coatings (TBCs) field for its excellent fracture toughness (≈2 $MPa{\cdot}m^{1/2}$) and resistance to sintering, has garnered significant attention for high-temperature abradable applications below 1200 °C [2,3]. With the addition of a polyester pore-former, porous YSZ ASCs show improved abradability with lower blade-tip wear [4–6]. However, when operating temperatures exceed 1200 °C, metastable tetragonal zirconia undergoes detrimental phase transformations that accelerate sintering and are accompanied by an increase in modulus, thereby leading to the poor service lifetime [7]. Given the ongoing trend of increasing gas turbine inlet temperatures to improve thrust-to-weight ratios, the demand for new ceramic-based abradable materials capable of withstanding temperatures up to 1300 °C is crucial.

$LaMgAl_{11}O_{19}$ (LMA) with a magnetoplumbite structure exhibits outstanding thermal stability up to 1600 °C, low thermal conductivity (0.8–2.6 $W{\cdot}m^{-1}{\cdot}K^{-1}$) and high fracture toughness (≈3.59 $MPa{\cdot}m^{1/2}$), and it is considered one of the most promising candidates

for next-generation TBC materials [8–10]. Therefore, imparting its abradability through a porous structure holds promise for achieving the excellent clearance control functionality of high-temperature ASCs. However, the porous LMA ASCs showed an uneven pore distribution with the presence of interconnected pores in our previous work [11]. Although this can improve abradability through the material removal mechanism to some extent, it also diminishes the cohesive strength, leading to heavy coating rupture during operation and ultimately affecting its durability [12,13]. It is also important to note that during the coating preparation process, thicker ASCs tend to develop significant thermal mismatch stress with the substrate. In addition, the presence of the amorphous phase in the as-sprayed coating can lead to shrinkage stress due to volume changes during high-temperature recrystallization [14]. These stresses are released through the formation of cracks in the coating. While vertical cracks are relatively stable, horizontal crack propagation can lead to delamination or even coating failure [15]. Therefore, interconnected pores and cracks in the coating have potential negative impacts on the service lifetime and abradable performance of ASCs. However, these defects can be adjusted and repaired through self-healing.

Self-healing methods in ceramic materials typically fall into two categories. The first method involves incorporating special materials capable of oxidation and glass formation at high temperatures. The oxides and glass phases produced fill cracks to achieve repair. The second method introduces sintering aids to accelerate the grain growth of the matrix materials under high-temperature conditions, thereby readjusting the internal defect distribution and structure [16]. For the former approach, early research focused on using SiC to repair cracks in mullite ceramics [17]. The healing process can be enhanced by adding a small amount of MnO, which lowers the viscosity of the oxide and promotes material flow [18]. Building on this concept, many researchers have developed self-healing composites that include SiC/spinel [19], SiC/ZrO_2 [20], SiC/Al_2O_3 [21,22], and others. In addition, Yuan et al. [23] utilized the volume expansion caused by the reaction between the oxide and the matrix material to promote crack closure. The latter method enhances diffusion coefficients by forming solid solutions or low-temperature liquid phases, facilitating the densification process [24]. For ASCs, which inherently contain relatively high proportions of the pores and cracks, using a single method may not achieve ideal self-healing effects. Therefore, combining these two methods is necessary.

Currently, a new class of materials has attracted great interest, known as MAX phase ceramics, particularly Ti_3AlC_2 (TAC) in the Ti-Al-C system. TAC combines numerous advantages of ceramics and metals, featuring low density, high toughness, high strength, and excellent resistance to thermal shock [25]. Due to its unique crystal structure and bonding mechanism, TAC exhibits the selective oxidation of highly reactive Al, forming a protective Al_2O_3-rich oxide layer that impedes further oxygen penetration [26]. However, in steam environment, TAC undergoes breakaway oxidation due to the enhanced mass-transport process, accelerated oxidation, and resulting growth stress, which can lead to the cracking or even spallation of the oxide layer [27,28]. The self-healing capability of TAC has been extensively investigated, where oxidation at high temperatures results in the formation of Al_2O_3 and rutile TiO_2. The accompanying volume expansion under compressive stress facilitates crack closure [29,30]. Notably, Chen et al. [31] studied the NiCrAlY/Cr_3C_2-TAC coating and found that the tribological performance was improved by the filling of oxide particles in the worn area. Additionally, while TiO_2 is commonly used as a sintering aid in the preparation of corundum ceramics due to its ability to dissolve into Al_2O_3, generating numerous cation vacancies that enhance ion diffusion rates and accelerate densification through solid-phase reaction mechanism, there has been limited research on the long-term thermal stability of the additives and their effects on the mechanical properties of the matrix material [32]. It is noteworthy that the layered structure of MAX phase ceramics imparts excellent self-lubricating properties, crucial for enhancing the abradable performance of matrix materials [33]. As reported by Zhao et al. [34], the lubrication of the tribofilm was improved by the addition of TAC and its oxides.

In this study, LMA was used as the matrix material, polyester as the pore-former, and TAC as both the self-healing agent and sintering aid. Initially, porous LMA-based composite coatings were prepared using the atmospheric plasma spraying (APS) process. Subsequently, the composite coatings underwent a self-healing process via high-temperature annealing at 1200 °C, and the effects of varying TAC contents on the self-healing performance were analyzed. Finally, the potential of the composite coatings as high-temperature ASCs was carefully investigated by analyzing the air oxidation and steam-corrosion behaviors at 1300 °C.

2. Methodology

LMA feedstock powder was prepared in-house by traditional solid-state reaction. A detailed description can be found elsewhere [35]. The LMA powders with different contents (0, 5, 10 and 20 wt.%) of TAC powders (200 mesh, 98%, Forsman Scientific Co., Ltd., Beijing, China) were ball-milled using zirconia balls for 72 h, then mechanically mixed with same content (10 wt.%) of polyester powder (400 mesh, 99%, Jiashan Furui Engineering Materials Co., Ltd., Jiashan, China), and finally spray-dried. The composite powder with particle size between 32 and 125 mm was collected and used directly for coating preparation without other treatments. Due to the similar densities of LMA and TAC (4.261 and 4.285 g/cm^3, respectively), their volume ratios and weight ratios were also nearly identical. In the following discussion, the composite powders and coatings are labeled L0T, L5T, L10T, or L20T depending on the TAC content.

The XRD patterns of the composite powders are shown in Figure 1. In addition to the LMA, the diffraction peaks of $LaAlO_3$, crystalline aromatic polyester and TAC also appeared. Among them, the $LaAlO_3$ phase often exists in LMA powder and coating as a secondary phase and is difficult to completely eliminate [8,10,35]. Furthermore, an unknown phase with a diffraction peak near 2θ = 30° has been observed and will be discussed in detail below. An interesting phenomenon is that with the increase in TAC content, the main peak near 2θ = 39° gradually broadened, indicating a reduction in TAC crystallite size during the ball-milling process. This reduction in crystallite size may contribute to an increased specific surface area, thereby enhancing its ability to oxidize and self-heal at high temperatures. All powders displayed similar microscopic morphologies. Taking L20T as an example, Figure 2 shows an SEM image and the EDS result of the composite powder. It can be observed that some powders are cladding particles, with fine LMA particles on the exterior and coarse polyester particles on the interior, along with some residual polyester (C element) on the particle surface. Additionally, the element mapping of Ti indicated that the distribution of TAC is relatively uniform, although some aggregation is observed. This was likely due to the layered structure of TAC, which made it difficult to completely pulverize during the ball-milling process.

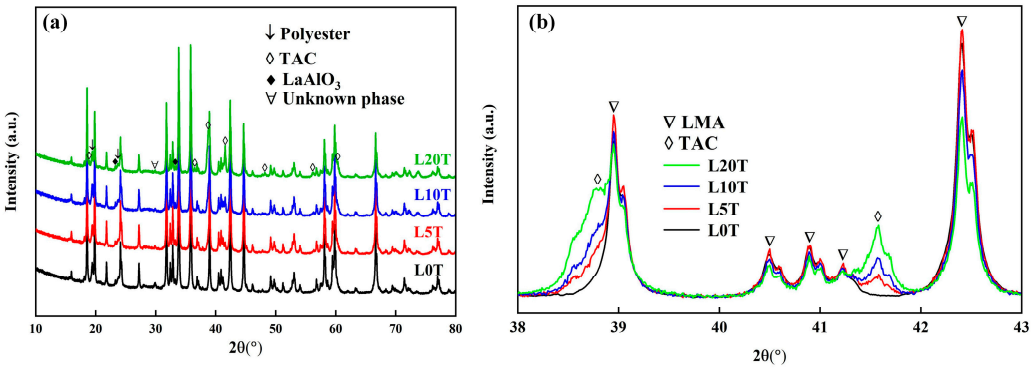

Figure 1. XRD patterns of the composite powders: (**a**) 2θ = 10–80° and (**b**) 2θ = 38–43°.

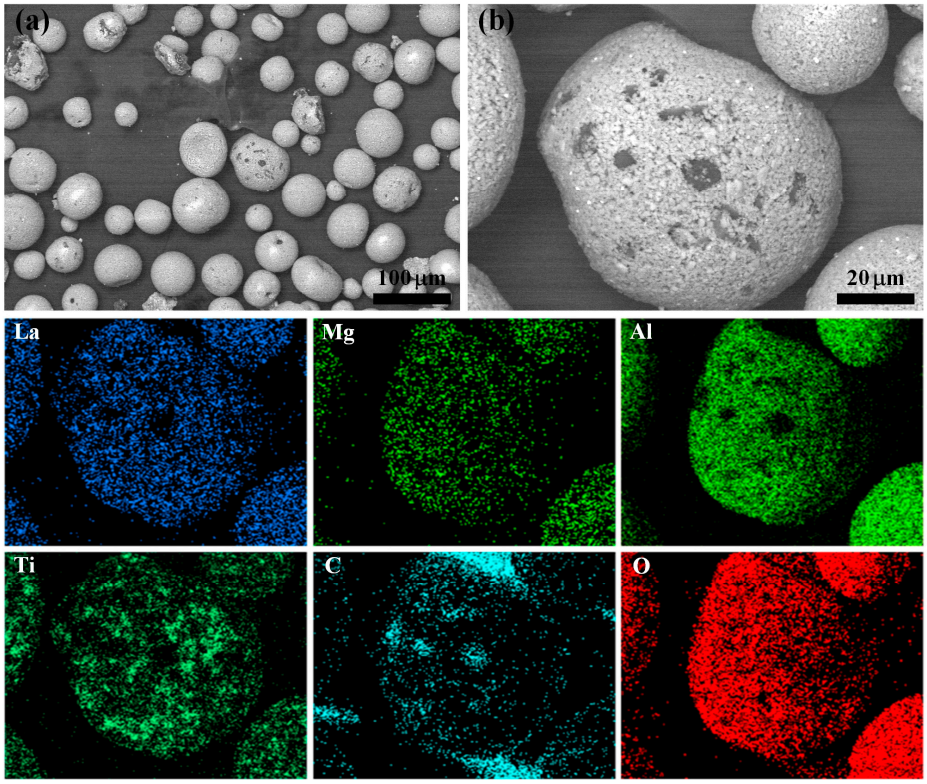

Figure 2. (**a**,**b**) SEM and EDS results of the L20T composite powder.

The free-standing coatings were used in this work, all of them prepared by the APS process and subsequent annealing procedure, as shown in Figure 3. Firstly, the composite powders were sprayed onto grit-blast roughened graphite substrates using a MultiCoat system (F4MB-XL gun, Oerlikon Metco, Wohlen, Switzerland) with an APS power of 28 kW, spraying distance of 130 mm and coating thickness of 1.5 mm. This spraying parameter is derived from our previous research on the LMA ASCs, which showed excellent isothermal oxidation and thermal shock resistance at 1300 °C [11]. To mitigate rapid cooling during the APS process, the plasma plume was employed to preheat the substrate surface to approximately 500 °C before powder feeding, with the temperature measured by an infrared thermometer. Secondly, the coated samples were cut into small pieces with a dimension of 15 mm × 15 mm, and later graphite substrates were mechanically removed. Finally, all coatings were subjected to 10 h at 1200 °C annealing in air, with heating and cooling rates of 5 °C/min, to achieve self-healing and recrystallization and to burn off polyester for pore-forming [14]. The selection of this annealing temperature is based on the recrystallization temperatures of the LMA material (900 °C and 1170 °C) [14]. At 1200 °C, TAC can also undergo significant oxidation, thereby contributing to its self-healing functionality [36].

In air-oxidation and steam-corrosion experiments, the free-standing coatings in the post-annealing state were placed in an alumina crucible and exposed to a lab air atmosphere and steam atmosphere at 1300 °C in Muffle furnace and tube furnace, respectively. The steam atmosphere with a volumetric ratio of 90% H_2O-10% O_2 was generated by a steam generator and then transported to the tube furnace [37,38]. For both experiments, four samples were initially oxidized simultaneously and weighed every 50 h. One sample was removed after 100 and 200 h, respectively, ensuring that at least three samples were involved in the weight measurement under each condition.

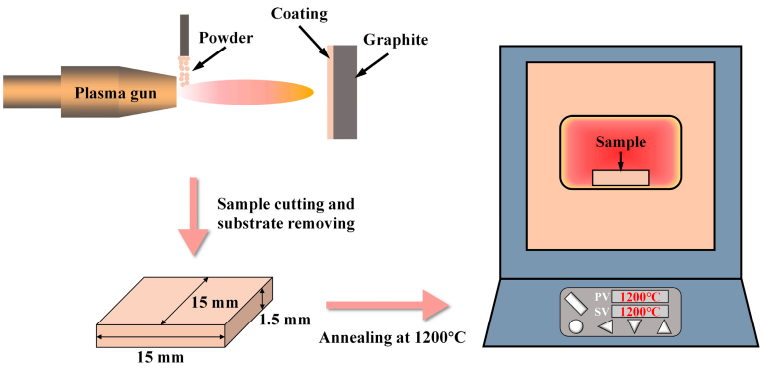

Figure 3. The preparation process and annealing of the free-standing composite coatings.

The phase compositions of the composite coatings after oxidation and corrosion for 100 and 200 h were identified by X-ray diffraction (XRD, Cu-Kα radiation, Rigaku SmartLab, Tokyo, Japan). The surface and cross-sectional morphology and elemental analysis of the oxidized samples were carried out in a scanning electron microscope (SEM, QUANTA FEG 450, Hillsboro, OR, USA) with energy dispersive spectroscopy (EDS, Xplore 30, Oxford Instruments, Oxford, UK). For cross-sectional observation, the cut samples needed to be cold-mounted in epoxy resin, cured for 24 h, and then polished to 1 µm with a diamond suspension. The porosity, crack ratio (the ratio of the crack area to the total area) and pore size distribution of the composite coatings were evaluated by ten back-scattered electron (BSE) images (magnification ×200) using ImageJ software (v.1.51). Density was measured using the Archimedes method, and the superficial Rockwell hardness was measured with a hardness tester (TH310, Time High Technology Co., Ltd., Beijing, China) using a 12.7 mm tungsten carbide ball, a dwell time of 10 s and a load of 15 kg.

3. Results and Discussion

3.1. LMA-Based Composite Coatings after Annealing at 1200 °C

The XRD patterns of the LMA-based composite coatings after annealing at 1200 °C are shown in Figure 4. For the better identification of phase transitions, XRD patterns in the 2θ range of 10–80° and 25–35° are displayed. It should be noted that the $LaTi_2Al_9O_{19}$ (LTA) phase arose as the addition of TAC in the L5T sample and became more prominent in the L10T and L20T samples in the post-annealing state, which was related to the oxidation of TAC, the formation of Al_2O_3 and rutile TiO_2, and the subsequent reaction with $LaAlO_3$ present in the coatings during spraying and annealing processes [39,40]:

$$4Ti_3AlC_2 + 23O_2 \rightarrow 12TiO_2 + 2Al_2O_3 + 8CO_2(g) \quad (1)$$

$$LaAlO_3 + 2TiO_2 + 4Al_2O_3 \rightarrow LaTi_2Al_9O_{19} \quad (2)$$

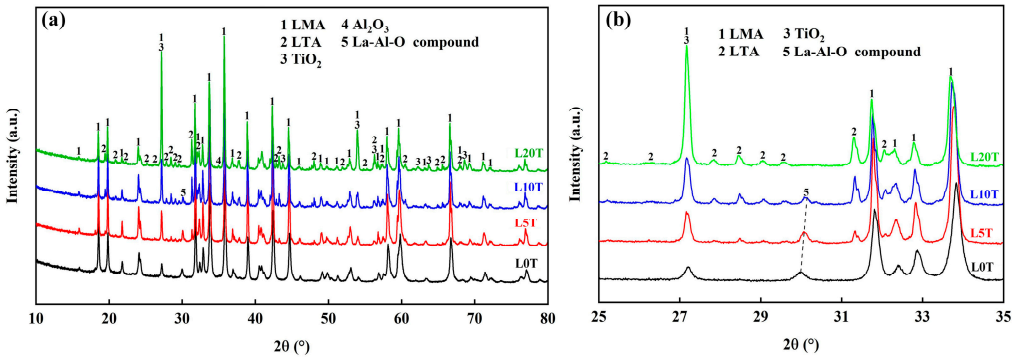

Figure 4. XRD patterns of the composite coatings after annealing at 1200 °C: (**a**) 2θ = 10–80° and (**b**) 2θ = 25–35°.

When the addition of TAC reached 20 wt.%, the diffraction peak near 2θ = 27° surged and the diffraction peak near 2θ = 30° disappeared. The peak near 2θ = 30° was also detected in our earlier works, but the specific phase composition could not be identified [41,42]. However, the peak intensity of an unknown phase (Figure 1) gradually decreased with the addition of TAC and it coexisted with Al_2O_3, as shown in Figure 4a [43]. Therefore, we can conclude that the unknown phase may be a La-Al-O compound, which can also react with rutile TiO_2 to form LTA and was gradually consumed with the increased addition and oxidation of TAC. The compound was depleted when TAC was added in excess of 10 wt.%, resulting in an excessive amount of residual rutile TiO_2 in the annealed L20T sample. Furthermore, the diffraction peak of the La-Al-O compound near 2θ = 30° slightly shifted toward the higher diffraction angle with the addition of TAC. This indicates that during the reaction with TiO_2, the compound primarily provided La^{3+} with a larger ionic radius, leading to lattice contraction and a decrease in the interplanar spacing.

Surface micrographs of the LMA-based composite coatings after annealing are shown in Figure 5. The surface of the TAC-free coating, as depicted in Figure 5a, exhibited numerous overlapped splats with typical thermal spraying characteristics formed by the spreading of molten droplets, along with clearly visible surface cracks [10]. In contrast, the composite coatings containing TAC, shown in Figure 5b–d, had rougher surfaces (arithmetic mean roughness Ra increased from 5 to 8 μm), significantly increased grain size, and more surface voids, but no surface cracks were observed. According to the literature [44,45], an appropriate amount of TiO_2 is typically introduced during the preparation of $MgAl_2O_4$ spinel ceramic to enhance density and strength. This increases the vacancy concentration in the spinel structure and activates the lattice through structural distortions caused by the substitution of Ti^{4+} for Al^{3+}, thereby promoting a sintering effect. The crystal structure of LMA is formed by alternating spinel planes composed of Al^{3+} and O^{2-} and mirror planes composed of La^{3+} and O^{2-}, similar to the $MgAl_2O_4$ [46]. Therefore, it can be concluded that the TiO_2 formed from the oxidation of TAC acted as a sintering aid in the composite coatings during annealing, resulting in stronger ion diffusion and faster grain growth. Additionally, Ti^{4+} (ionic radius 0.0605 nm) can replace Al^{3+} (ionic radius 0.0535 nm) in the spinel plane, leading to lattice expansion and increased interplanar spacing, which is consistent with the shift of the LMA diffraction peaks to lower angles observed in Figure 4b.

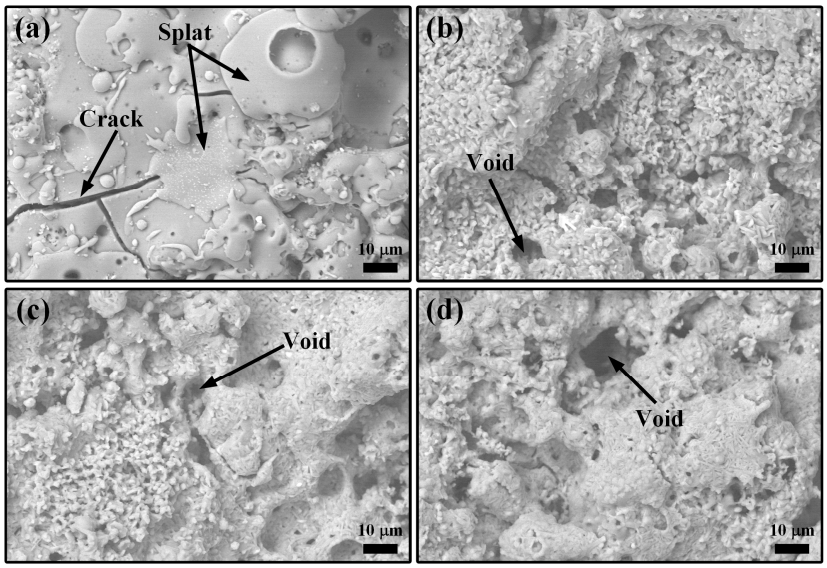

Figure 5. Surface SEM images of the composite coatings after annealing at 1200 °C: (**a**) L0T; (**b**) L5T; (**c**) L10T; (**d**) L20T.

Figure 6 shows the cross-section SEM images of LMA-based composite coatings after annealing. As shown in Figure 6a–a″, the L0T sample exhibited numerous cracks and un-melted particles after annealing at 1200 °C, along with large pores left by the

removal of polyester particles and small pores formed due to the insufficient spreading of molten droplets during spraying. The pore distribution was relatively random, with many interconnected pores. Additionally, the coating contained numerous white contrast areas, which are difficult to observe due to their small size. As depicted in Figure 6b–b″, a TAC content of 5 wt.% resulted in a distinct increase in grain size, more pronounced grain boundaries, wider crack openings, and the appearance of additional small pores. Due to the presence of a mirror plane in the LMA crystal structure, the diffusion along the *c*-axis is slow, causing grains to preferentially grow along the *a* and *b* axes, resulting in a platelet-like grain morphology for LMA [14]. The rearrangement of grains during exposure to high temperature promoted the LMA grain growth, leading to wider crack openings and the formation of small pores due to the limited contact area between the platelet-like grains. Importantly, as seen in Figure 6b″, the white contrast areas within the coating appeared to have aggregated, with EDS point scanning results indicating that these areas mainly contain La, Al, and O elements. As shown in Figure 6c–c″, when the TAC content increased to 10 wt.%, the grains did not continue to grow, the crack openings became smaller, and the white contrast areas within the coating decreased. When the TAC content was further increased to 20 wt.%, as shown in Figure 6d–d″, the cross-section became relatively flat, with cracks and white contrast areas disappearing, and the small pores distributed uniformly, indicating a significant self-healing effect. The changes of the white contrast areas in the microstructure correspond to the changes in the intensity of the unknown phase diffraction peak near $2\theta = 30^\circ$ in Figure 4b, further confirming that it is the La-Al-O compound. Table 1 presents the EDS map scanning results of the coating cross-section at 200× magnification. The atomic percentage of Ti increased from L5T to L20T, correlating with the TAC addition levels and corresponding to the incremental intensity of the TiO_2 diffraction peak observed in Figure 4. Meanwhile, the atomic percentages of La, Mg, and Al gradually decreased. Furthermore, based on the calculation from Equation (1), the oxidation process results in approximately a 1.5-fold volume expansion. Therefore, it can be inferred that with low TAC content (L5T), the oxidation generates relatively small amounts of TiO_2 and Al_2O_3, mildly promoting LMA grain growth and subsequently reacting to form LTA. In contrast, with increased TAC content (L10T and L20T), the excessive oxidation products undergo significant volume expansion, filling cracks within the coating. Moreover, the continuous promotion of sintering by TiO_2 results in significant crack closure, thereby achieving self-healing functionality.

Figure 7a,b illustrates the porosity, density and hardness of the composite coatings after annealing. The TAC-free coating exhibited a porosity of $31.11 \pm 1.21\%$, a density of 3.1 ± 0.32 g/cm^3 and a hardness of 68.33 ± 3.21 HR15Y. With a 5 wt.% TAC addition, the porosity and hardness increase, while the density decreases to $39.02 \pm 1.75\%$, 70.18 ± 2.06 HR15Y and 2.9 ± 0.33 g/cm^3, respectively. As TAC content continued to increase, the porosity gradually decreased, while the density and hardness increased, reaching $32.17 \pm 0.94\%$, 3.4 ± 0.22 g/cm^3 and 74.88 ± 1.55 HR15Y for the L20T sample. Figure 7c,d shows the crack ratio and pore size distribution of the composite coatings after annealing. The trend in the crack ratio was consistent with that of porosity, both peaking at L5T and then gradually decreasing with the addition of TAC. The pore morphology primarily featured small pores with a diameter of 3–5 μm and large pores with a diameter of 30–60 μm. In the L5T samples, the proportion of small pores is maximized while the proportion of large pores is minimized. Conversely, the L20 samples exhibit the highest proportion of large pores. These changes align closely with the microstructural variations observed in Figure 6. The addition of a small amount of TAC facilitated the neck growth and sintering-induced shrinkage of LMA grains, resulting in the formation of small pores and microcracks that increased porosity and decreased density [47]. With further TAC addition, excessive TiO_2 promoted the densification process of the coating. This ultimately led to the effective healing of cracks and the transition from small pores to larger ones. Moreover, the increased hardness of the composite coatings can be attributed to the effect of the newly formed harder LTA, TiO_2, and Al_2O_3 phases, while the standard deviation was reduced due to the improved

uniformity of the coating structure [10,48]. The rise in hardness following the addition of TAC was expected. While this is anticipated to reduce abradability, we also hoped it would enhance durability. Striking a balance between these two properties is necessary, as it is impossible to optimize both simultaneously. Fine-tuning the proportions of LMA, TAC, and polyester may yield a better overall performance of the composite coatings, which requires further experimental validation.

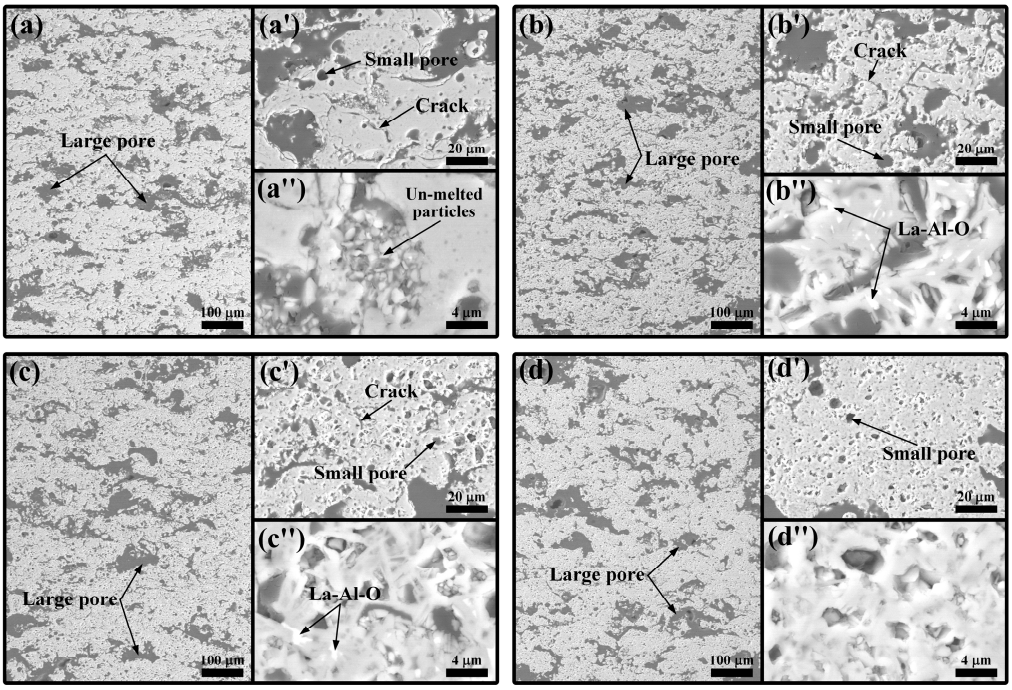

Figure 6. Cross-section SEM images of the composite coatings after annealing at 1200 °C: (**a**–**a′′**) L0T; (**b**–**b′′**) L5T; (**c**–**c′′**) L10T; (**d**–**d′′**) L20T.

Table 1. The atomic percentage of main elements in composite coatings after annealing at 1200 °C.

Sample	La L	Mg K	Al K	Ti K	O K
L0T	4.55	3.32	41.39	-	50.74
L5T	3.98	2.88	37.49	2.21	53.44
L10T	3.65	2.49	35.24	4.23	54.39
L20T	2.66	1.83	27.70	8.84	58.97

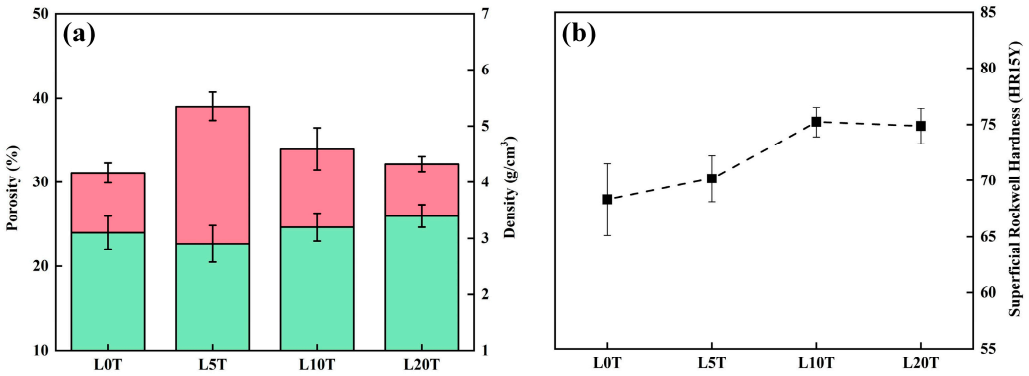

Figure 7. *Cont.*

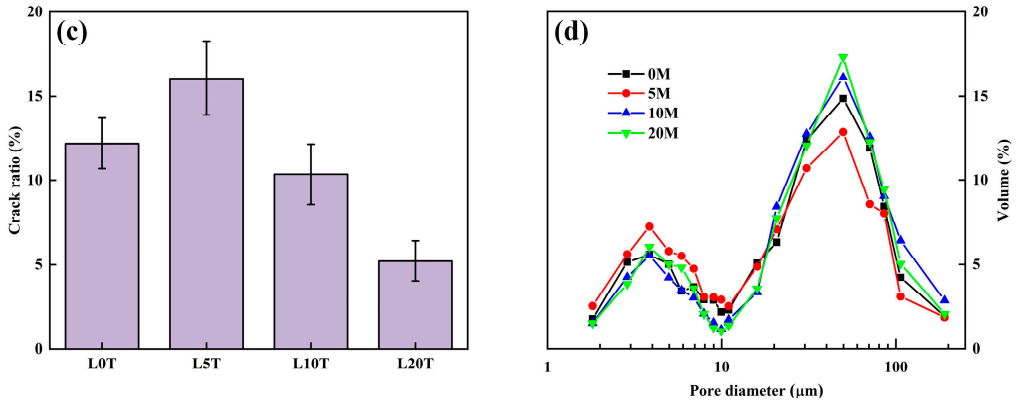

Figure 7. Porosity and density (**a**), hardness (**b**), crack ratio (**c**) and pore size distribution (**d**) of the composite coatings after annealing at 1200 °C. The red bars indicate porosity, and the green bars represent density in (**a**).

3.2. LMA-Based Composite Coatings after Air Oxidation at 1300 °C

The weight change of the composite coatings after air oxidation at 1300 °C is shown in Figure 8. The L0T sample remained relatively stable during air oxidation, while the addition of TAC resulted in a weight gain for the composite coatings. This may be due to trace amounts of TAC remaining in the composite coatings after annealing at 1200 °C, which continued to oxidize at 1300 °C. This phenomenon occurs because TAC particles undergo selective oxidation at high temperatures, forming a protective Al_2O_3 scale on their surface, which slows down the oxidation rate of the particle interiors [49]. The L5T sample follows a parabolic oxidation process, gaining 0.10% after 200 h of air oxidation. In contrast, the L10T and L20T samples exhibited linear changes, with weight gains of 0.21% and 0.18%, respectively, after 200 h. The L10T sample exhibited the highest oxidation rate, suggesting the possible presence of the most residual TAC after annealing. According to the literature [50], as the Al content decreases, selective oxidation may gradually transition to breakaway oxidation, leading to the oxidation of Ti and C and causing the Al_2O_3 scale to gradually lose its protective capacity. Therefore, it is speculated that the excessive TiO_2 generated during the annealing of the L20T sample may have induced Al depletion and breakaway oxidation, resulting in relatively lower residual TAC than the L10T sample. Detailed analysis is needed to determine the specific causes behind these observations.

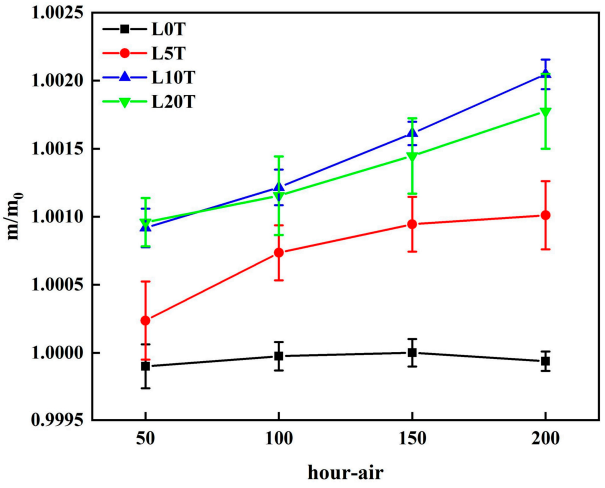

Figure 8. Weight change of the composite coatings after air oxidation at 1300 °C.

Figure 9 shows the XRD patterns of the composite coatings after 100 and 200 h of air oxidation at 1300 °C, compared with the samples after annealing at 1200 °C. As shown in Figure 9a, the diffraction peak intensities of LMA and La-Al-O increased in the TAC-free

coatings, indicating that the residual amorphous phase underwent more complete recrystallization at 1300 °C. Additionally, the diffraction peaks of the $LaAlO_3$ phase appeared. Given that the plasma-sprayed $LaAlO_3$ coating can recrystallize at temperatures as low as 1100 °C, it is suggested that $LaAlO_3$ might have been partially covered by residual amorphous LMA, leading to it being below the detection limit [51]. As shown in Figure 9b, the L5T sample exhibited an increase in LMA peak intensity with a corresponding shift to lower angles after air oxidation, indicating LMA grain growth. Moreover, no diffraction peaks of $LaAlO_3$ and rutile TiO_2 were observed, suggesting that they had completely reacted to form LTA. In the L10T sample, different phenomena were observed, as shown in Figure 9c. Firstly, the peak intensities representing LMA and rutile TiO_2 around $2\theta = 27°$ decreased gradually after air oxidation, with peak shifts greater than those in the L5T sample. Secondly, the peak intensity representing the La-Al-O compound around $2\theta = 30°$ significantly decreased, and new peaks corresponding to $La_4Ti_3O_{12}$ appeared. In the first phenomenon, due to the excellent high-temperature phase stability of LMA, the decrease in peak intensity may be attributed to the consumption of TiO_2 within the coating during air oxidation, while the significant peak shifts could be associated with abnormal grain growth of LMA. To investigate the underlying cause of the latter phenomenon, an analysis was conducted using the La_2O_3-TiO_2-Al_2O_3 ternary phase diagram, as shown in Figure 10. It reveals the presence of five phases across different ratios of La_2O_3 and TiO_2, with the $La_4Ti_3O_{12}$ phase forming only at a 2:3 ratio. Moreover, the presence of Al^{3+} prioritizes the formation of LTA until all Al^{3+} is consumed. Additionally, Equation (2) indicates that the consumption of Al_2O_3 in the process of forming LTA doubles that of TiO_2. In summary, the L10T sample first formed LTA during air oxidation, followed by a further reaction of the excessive La-Ti-O system to produce $La_4Ti_3O_{12}$, resulting in a gradual decrease in the peak intensities of the TiO_2 phase and La-Al-O compound. As shown in Figure 9d, the L20T sample only detected the presence of the LMA, LTA, and excessive TiO_2 phases after air oxidation. No variation in TiO_2 peak intensity was observed with oxidation time, indicating that the L20T sample stabilized after annealing at 1200 °C and maintained excellent stability during air oxidation at 1300 °C.

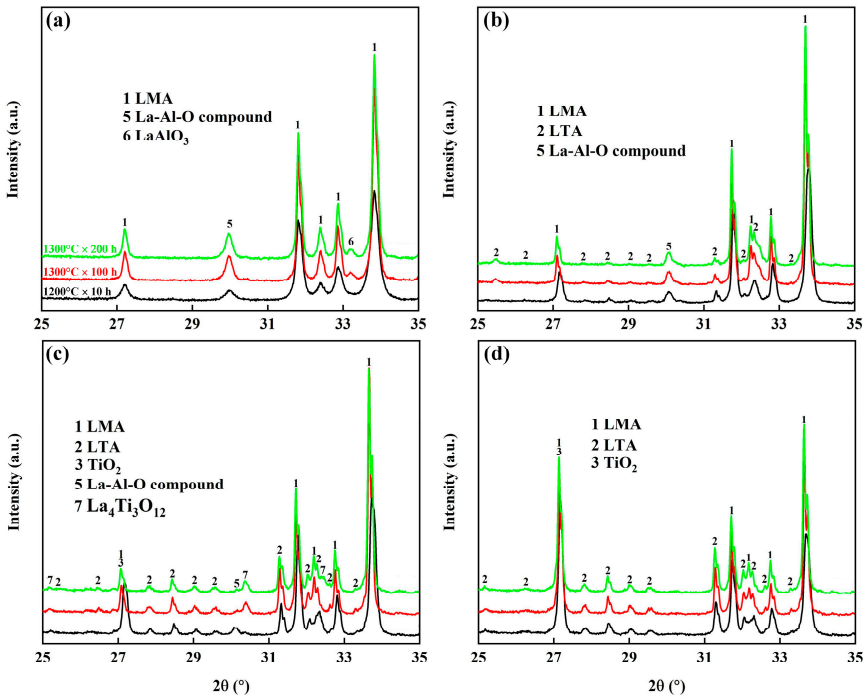

Figure 9. XRD patterns of the composite coatings after annealing at 1200 °C and air oxidation at 1300 °C: (**a**) L0T; (**b**) L5T; (**c**) L10T; (**d**) L20T. From bottom to top showing the samples subjected to 10 h annealing, 100 and 200 h air oxidation.

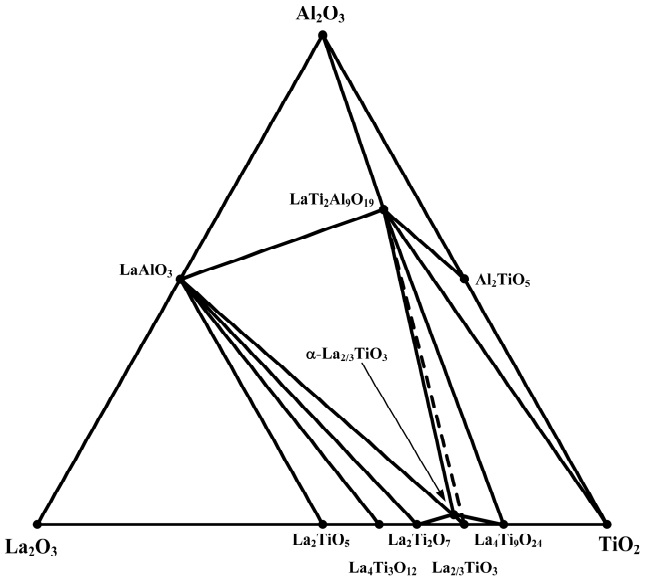

Figure 10. La_2O_3-TiO_2-Al_2O_3 ternary phase diagram. Derived from [52,53].

Figure 11 depicts the surface SEM images of the composite coatings after air oxidation at 1300 °C, while Table 2 presents the average thickness and aspect ratio of LMA grains. As shown in Figure 11a,a′, the L0T sample retained a similar surface morphology to that after annealing, characterized by numerous un-melted particles and cracks, with no significant grain growth or crack closure observed. In Figure 11b,b′, the L5T sample exhibited noticeable grain growth with a high aspect ratio after air oxidation. The aspect ratio decreased from 7.53 after 100 h to 6.33 after 200 h, while the grain thickness increases to 1.15 μm. Figure 11c–d′ illustrates that both L10T and L20T samples exhibited similar trends after air oxidation. Initially, there was a notable acceleration in the rate of grain growth, with platelet-like grains reaching thicknesses exceeding 2 μm after 100 h, followed by slower growth after 200 h. Additionally, the aspect ratio of platelet-like grains decreased to around 4, transitioning gradually towards equiaxed grains, with the occasional abnormal growth of larger grains up to approximately 20 μm in size. These observations indicate that while a lower addition of TAC (L5T) accelerated the sintering of LMA, the effect was limited due to the lower content of TiO_2 and the eventual formation to LTA. On the other hand, higher TAC additions (L10T and L20T) resulted in an excess of TiO_2 within the coatings, which continuously promoted the diffusion along the c-axis and led to a significant increase in grain thickness. Compared to the L10T sample, the L20T sample exhibited greater grain thickness after air oxidation but a smaller aspect ratio, indicating the slower longitudinal growth of grains. Considering the lower porosity and higher density of the L20T sample after annealing (Figure 7), the limited growth space for grains led to compression-induced stacking between them. However, the abnormally grown large grains observed in Figure 11c′ appear not to have formed from the stacking of smaller grains. These are likely corresponding to LTA grains due to their crystal structure being four times that of the LMA structure, which tends to form larger grains. It should be noted that the transformation of platelet-like grains into equiaxed grains may weaken the bridging effect, potentially compromising its toughening behavior [46].

Due to the minor microstructural differences between samples after 100 and 200 h of air oxidation, only cross-sectional SEM images taken after 200 h are shown, as depicted in Figure 12. Similarly, owing to the excellent sintering resistance of LMA at 1300 °C, the cross-sectional morphology of the L0T sample remained largely unchanged after air oxidation, as shown in Figure 12a–a″. The L5T sample exhibited numerous elongated pores originating from cracks, associated with the formation of platelet-like grains with high aspect ratios (Figure 12b–b″). The stacking of these grains occurred primarily in parallel directions, resulting in slower growth in the thickness direction of both sides of the crack

openings due to smaller contact areas. In addition, clustered small grains were observed in the gaps between platelet-like grains, possibly originating from the un-melted particles. Insufficient TiO_2 within the coating made it difficult to promote the contact and growth of these particles during air oxidation. For the L10T and L20T samples with excessive TiO_2 content, as shown in Figure 12c–d″, rapid grain growth in the thickness direction during air oxidation led to the filling of elongated pores, ultimately forming rounded micro-pores. In the L10T sample, smaller equiaxed grains also appeared between larger grains, subjected to compression from surrounding grains. In the L20T sample, the close stacking of platelet-like grains along similar growth directions effectively eliminated pores. However, compared to the annealed sample (Figure 6d–d″), the pore size in the L20T sample significantly increased after air oxidation due to the inadequate stacking of some grains with different orientations, and the abnormal growth of a few large grains within the coating further hindered contact between smaller grains.

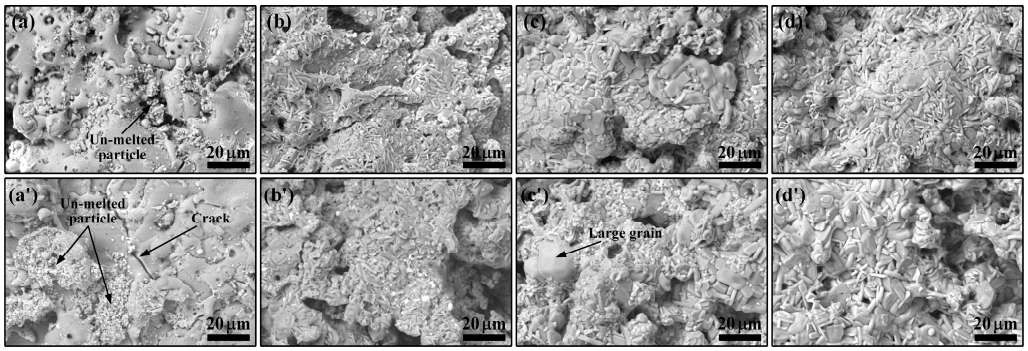

Figure 11. Surface SEM images of the composite coatings after (**a**–**d**) 100 h and (**a′**–**d′**) 200 h air oxidation at 1300 °C; (**a**,**a′**) L0T, (**b**,**b′**) L5T, (**c**,**c′**) L10T, (**d**,**d′**) L20T.

Table 2. Average thickness and aspect ratio of LMA grains after annealing and air oxidation.

Treatment Condition	L5T		L10T		L20T	
	Thickness (μm)	Aspect Ratio	Thickness (μm)	Aspect Ratio	Thickness (μm)	Aspect Ratio
1200 °C × 10 h	0.74	3.52	0.84	7.07	0.81	6.58
1300 °C × 100 h	0.87	7.53	2.04	4.08	2.26	3.96
1300 °C × 200 h	1.15	6.33	2.24	4.76	2.41	4.54

Figure 13 shows the variation in porosity and density of the composite coatings after air oxidation, compared with the annealed samples. For the L5T sample, the porosity significantly decreased to 33.98 ± 1.5% after 200 h of air oxidation; L10T showed a slight decrease to 31.99 ± 2.6%; whereas L20T exhibited an increase in porosity to 36.09 ± 2.05%. These trends correspond with microstructural changes, with a significant sintering effect caused by high TAC content leading to abnormal grain growth and the emergence of equiaxed grains, thereby increasing porosity. It is noteworthy that the density of all coatings gradually increased after air oxidation, possibly influenced by the measurement method. Density was measured using the Archimedean principle. However, the increased proportion of closed pores within the composite coatings due to sintering can lead to artificially higher density measurement values. Ceramic-based ASCs are typically applied at high temperatures, often increasing porosity to reduce coating hardness and improve abradability, albeit with challenges in achieving uniform pore distribution, leading to randomly interconnected pores. Interconnected pores can compromise coating integrity by potentially causing through-coating damage. However, significant grain growth occurred in the LMA-based composite coatings studied here during high-temperature oxidation, transforming interconnected pores into closed pores, which enhances the cohesion of the coating. Additionally, cracks within the coating were also closed, effectively preventing

further crack propagation. Importantly, the L20T sample exhibited the most stable characteristics, with minimal changes in both phase composition and microstructure. Additionally, the coating porosity of the L20T sample increased with oxidation time, which is promising for ensuring the long-term abradable performance of the ASCs.

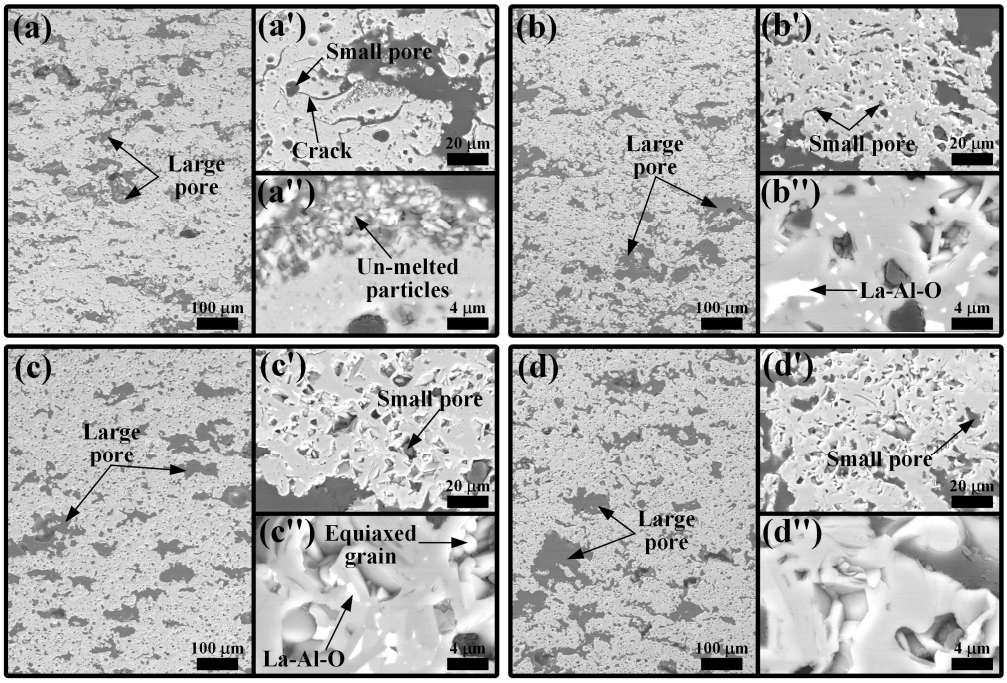

Figure 12. Cross-section SEM images of the composite coatings after 200 h air oxidation at 1300 °C: (**a**–**a′′**) L0T; (**b**–**b′′**) L5T; (**c**–**c′′**) L10T; (**d**–**d′′**) L20T.

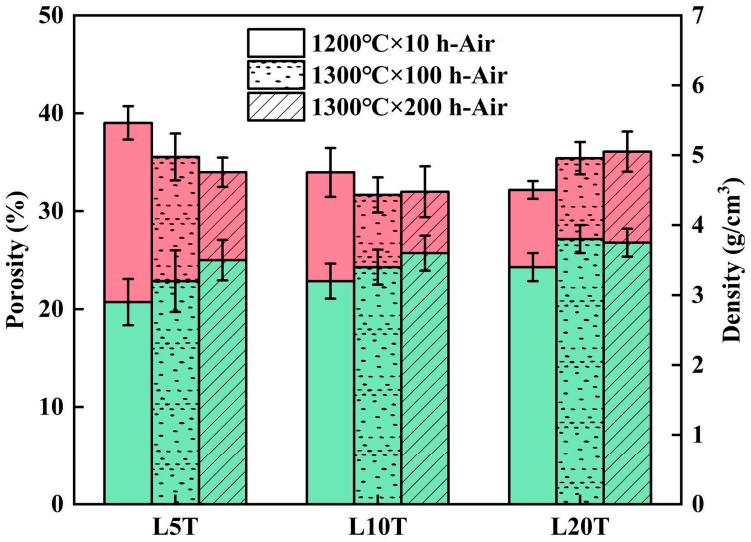

Figure 13. Changes of porosity and density of the composite coatings after annealing at 1200 °C and air oxidation at 1300 °C. The red bars indicate porosity, and the green bars represent density.

3.3. LMA-Based Composite Coatings after Steam Corrosion at 1300 °C

The weight changes of the composite coatings after steam corrosion at 1300 °C are shown in Figure 14, indicating that all samples experienced weight loss during the steam-corrosion process. The weight losses of the L0T and L20T samples were relatively similar, decreasing by 0.25% and 0.31%, respectively, after 200 h. The L5T sample exhibited the most severe weight loss, with a reduction of 0.89% after 200 h. The weight loss of the L10T sample was intermediate, decreasing by 0.61% after 200 h. Figure 15 presents the

XRD patterns of the composite coatings after steam corrosion at 1300 °C for 100 and 200 h, compared with the annealed samples. As shown in Figure 15a, in the L0T sample after steam corrosion, besides the presence of the LMA phase, a monoclinic phase La_2O_3 was detected, and the diffraction peaks of the $LaAlO_3$ phase disappeared. It is hypothesized that $LaAlO_3$ decomposes in the high-temperature steam-corrosion environment according to the following reaction:

$$2LaAlO_3 + 3H_2O\ (g) \rightarrow La_2O_3 + 2Al(OH)_3(g) \quad (3)$$

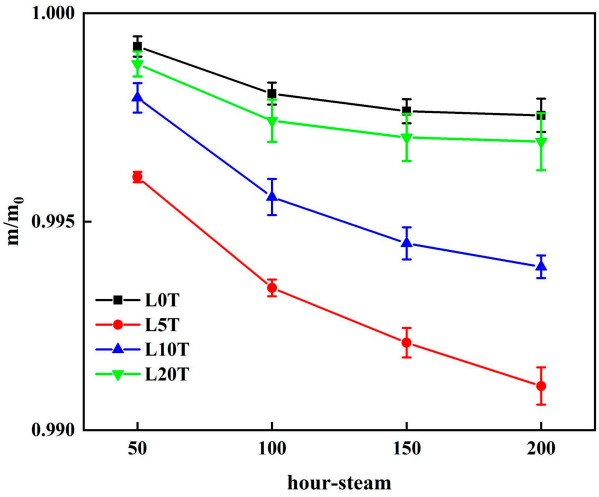

Figure 14. Weight change of the composite coatings after steam corrosion at 1300 °C.

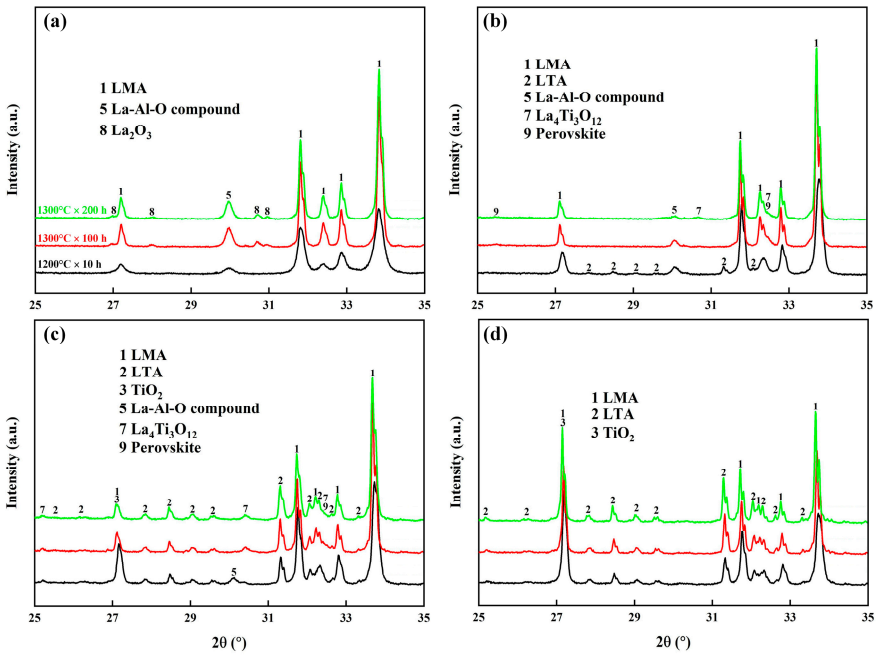

Figure 15. XRD patterns of the composite coatings after annealing at 1200 °C and steam corrosion at 1300 °C: (**a**) L0T; (**b**) L5T; (**c**) L10T; (**d**) L20T. From bottom to top showing the samples subjected to 10 h annealing, 100 and 200 h steam corrosion.

As shown in Figure 15b, the LTA phase disappeared in the L5T sample after steam corrosion, and the diffraction peaks corresponding to the $La_4Ti_3O_{12}$ phase and a perovskite-type phase emerged. With the progression of steam corrosion, the content of the $La_4Ti_3O_{12}$ phase increased, while the content of the perovskite-type phase decreased. According to the La_2O_3-TiO_2-Al_2O_3 ternary phase diagram in Figure 10, it can be observed that there

exists an A-site-deficient perovskite, $La_{2/3}TiO_3$, which is inherently unstable. However, doping it with 4 mol% $LaAlO_3$ can effectively stabilize this phase, forming a 4%$LaAlO_3$–96%$La_{2/3}TiO_3$ (α-$La_{2/3}TiO_3$) solid solution [53]. It is therefore speculated that during steam corrosion, the selective volatilization of Al caused the LTA phase to gradually decompose, forming the α-$La_{2/3}TiO_3$ phase. Subsequently, the further decomposition of α-$La_{2/3}TiO_3$ led to the formation of the $La_4Ti_3O_{12}$ phase. This series of decomposition processes resulted in significant weight loss in the L5T sample. Xie et al. [54] also observed the decomposition behavior of the LTA coating, noting the formation of α-$La_{2/3}TiO_3$ and Al_2O_3 on the surface of the LTA coating during burner flame testing. However, the presence of steam facilitated the further reaction of Al_2O_3 in this study, leading to the formation of gaseous $Al(OH)_3$, which subsequently volatilized. For the L10T sample, as shown in Figure 15c, the high TAC content resulted in a substantial amount of LTA within the coating. Although diffraction peaks of the $La_4Ti_3O_{12}$ and perovskite-type phase appeared, the LTA phase remained present. In the case of the L20T sample after steam corrosion, as depicted in Figure 15d, the XRD pattern only displayed peaks corresponding to the LMA, LTA, and rutile TiO_2 phases, which is consistent with the phase composition observed after air oxidation (Figure 9). Despite the weight loss observed in the L20T sample after steam corrosion, no peaks for α-$La_{2/3}TiO_3$ and $La_4Ti_3O_{12}$ were detected, possibly due to their concentrations being below the detection limit. Compared to L5T, the L10T and L20T samples exhibited lower weight loss, indicating a slower decomposition rate of LTA. This can be attributed to the smaller grain size in the L5T sample after annealing, which results in a larger specific surface area and more grain boundaries with high reactivity, making it more vulnerable to steam corrosion. Conversely, the larger grain sizes in L10T and L20T reduced their reactivity, providing greater resistance to steam corrosion. Furthermore, as seen in Figure 7, the L5T sample had the highest porosity and the lowest density after annealing. The porosity decreased and density increased for the L10T and L20T samples, indicating that the densification of the composite coatings effectively hindered the corrosion penetration, thereby slowing the decomposition of LTA within the coatings.

Figure 16 illustrates the surface SEM images of the composite coatings post-steam corrosion, while Table 3 details the average thickness and aspect ratio of the LMA platelet-like grains. As shown in Figure 16a,a′, the L0T sample surface after steam corrosion displayed numerous platelet-like grains with slight crack closure. This differs from the morphology changes observed during static air oxidation and can be attributed to the accelerated mass transfer induced by steam atmosphere [55]. During this process, the LMA nanocrystals formed through recrystallization underwent bonding, convergence, and rearrangement, ultimately leading to significant grain growth and coarsening [56]. Despite this, a substantial number of un-melted particles remained, likely due to a limited contact area, restricting mass transfer. Additionally, La_2O_3 particles were observed on the L0T surface, appearing as large equiaxed grains with white contrast, aligning with the XRD results. The aspect ratio of the platelet-like grains was difficult to measure due to their encapsulation by surrounding particles. As depicted in Figure 16b,b′, the L5T sample after steam corrosion exhibited tightly stacked grains with clear grain boundaries, thus eliminating cracks, and numerous surface voids appeared. The high aspect ratio of 8.04 for the platelet-like grains after 100 h, as noted in Table 3, further indicates the rapid grain growth. For the L10T and L20T samples, see Figure 16c–d′, the grain morphology post-air oxidation and steam corrosion was similar, but the thickness of the platelet-like grains increased in the steam environment, while the aspect ratio decreased, indicating a transition towards equiaxed grains. Additionally, no abnormally large grains were observed on the coating surfaces after steam corrosion. Combined with the XRD results, this suggests that the corresponding phase was LTA, which decomposed during the steam-corrosion process. It is noteworthy that a considerable number of fine grains remained in the composite coatings. Prolonged high-temperature exposure might result in continued grain growth.

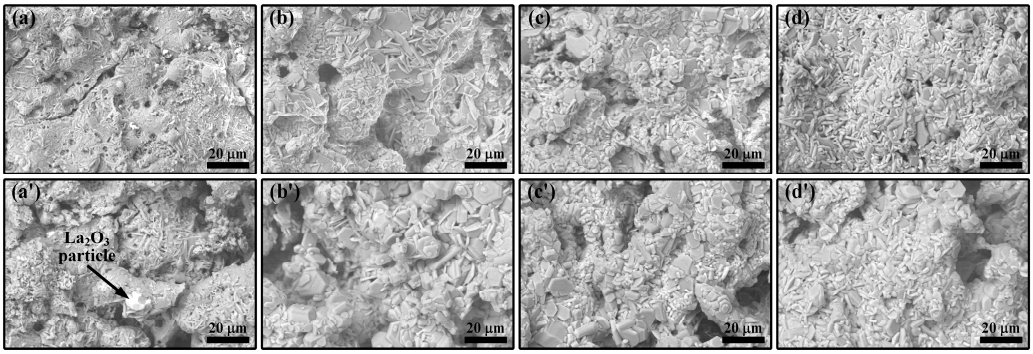

Figure 16. Surface SEM images of the composite coatings after (**a**–**d**) 100 h and (**a′**–**d′**) 200 h steam corrosion at 1300 °C; (**a**,**a′**) L0T, (**b**,**b′**) L5T, (**c**,**c′**) L10T, (**d**,**d′**) L20T.

Table 3. Average thickness and aspect ratio of LMA grains after steam corrosion.

Treatment Condition	L5T		L10T		L20T	
	Thickness (μm)	Aspect Ratio	Thickness (μm)	Aspect Ratio	Thickness (μm)	Aspect Ratio
1300 °C × 100 h	1.58	8.04	2.52	3.35	2.72	3.46
1300 °C × 200 h	1.96	7.77	2.69	4.16	2.80	4.01

The cross-sectional SEM images of the composite coatings after steam corrosion are depicted in Figure 17, with corresponding EDS map scanning results at 200× magnification detailed in Table 4. As shown in Figure 17a′–d′, after 200 h of steam corrosion, no obvious porous corrosion layer formed on the coating surface due to the selective volatilization of Al. However, compared to the relatively stable L0T and L20T samples, the surfaces of L5T and L10T samples exhibited rougher profiles, attributed to the significant decomposition of LTA on the surface. In addition, L5T and L10T samples displayed numerous fine grains on their surfaces, which are more susceptible to decomposition in a steam-corrosion environment due to their larger specific surface area. In L0T samples, as observed in Figure 17a–a″, grain growth was confined to the surface, with minimal microstructural changes within the coatings during steam corrosion, maintaining visible pores, cracks, and un-melted particles. Notably, the area of un-melted particles near the surface decreased, with some particles showing mutual adhesion and accumulation, induced by the movement of the grain boundary during sintering. A comparison of L5T, L10T, and L20T samples after 100 and 200 h of steam corrosion, as illustrated in Figures 17b–d and 17b″–d″, revealed a more pronounced presence of grain boundaries and larger gaps between grains within the coating microstructure compared to samples after air oxidation (Figure 12), indicating that steam also caused corrosion within the coating interior. For the relatively dense environmental barrier coatings (EBCs), exposure to steam environment initiates corrosion processes from the surface inward, concurrently forming a porous corrosion product layer on the coating surface. This phenomenon arises because the dense structure of the coating restricts the penetration of corrosive agents inward, relying instead on a slow diffusion mechanism to enter the coating interior [57,58]. However, the porous structure inside the ASCs provides pathways for the ingress of corrosive agents, facilitating their permeation throughout the entire coating structure. Analysis of the element proportions inside the composite coatings after 200 h of steam corrosion, as shown in Table 4, revealed the increased proportions of La and Ti elements and decreased Al element proportions compared to those before steam corrosion (see Table 1). Furthermore, L5T and L10T samples exhibited greater changes, consistent with the appearance of perovskite and $La_4Ti_3O_{12}$ phases in the XRD results. Interestingly, there was a slight decrease in Mg element proportions after steam corrosion, indicating the slight corrosion of LMA. It is noteworthy that despite undergoing corrosion, XRD analysis (Figure 15) showed no significant changes in the crystalline structure of LMA. This can be attributed to the formation of the magnetoplumbite-type structure in LMA,

which is not strictly dependent on perfect stoichiometric matching among its components. Even with slight variations in the Mg and Al ratios, a non-stoichiometric LMA can still exhibit a magnetoplumbite-type structure [59].

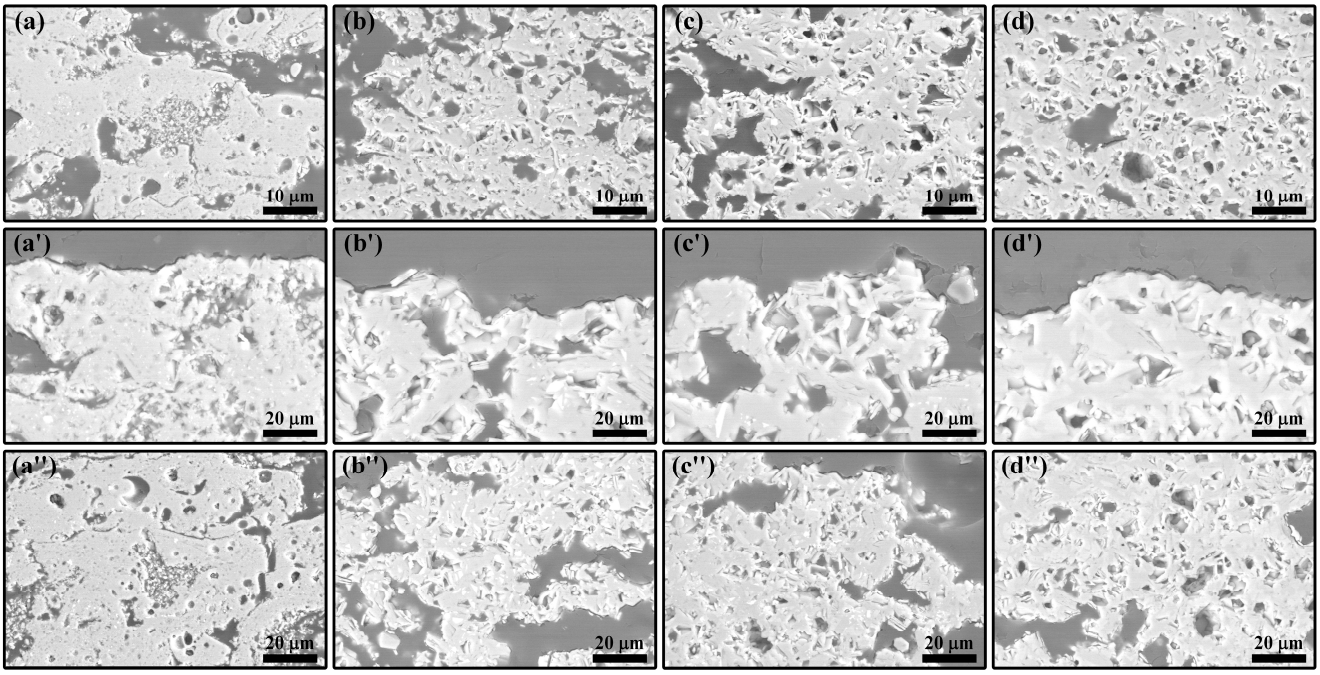

Figure 17. Cross-section SEM images of the composite coatings after (**a**–**d**) 100 and (**a′**–**d′′**) 200 h steam corrosion at 1300 °C; (**a**–**a′′**) L0T, (**b**–**b′′**) L5T, (**c**–**c′′**) L10T, (**d**–**d′′**) L20T.

Table 4. The atomic percentage of main elements in composite coatings after steam corrosion.

Sample	La L	Mg K	Al K	Ti K	O K
L0T	4.74	3.19	37.91	-	54.56
L5T	4.27	2.77	31.56	2.74	58.85
L10T	3.93	2.35	28.86	4.86	60.32
L20T	2.81	1.74	24.13	9.21	62.11

Figure 18 depicts the variation in porosity and density of the composite coatings after steam corrosion, compared with samples subjected to annealing. For the L5T sample, the porosity decreased and density increased post-steam corrosion, albeit to a lesser extent than observed in air oxidation (Figure 13). In the case of the L10T sample, porosity increased and density decreased after 100 h of steam corrosion, with a reversal of the trends observed after 200 h. The porosity and density changes in the L20T sample after steam corrosion were similar to those observed in the samples after air oxidation. In a high-temperature steam environment, the changes in coating porosity and density are influenced by two main factors: grain growth due to sintering and component volatilization caused by steam corrosion. However, sintering aided by the TiO_2 additive in the composite coatings may occur relatively quickly, whereas steam corrosion is a continuous process. Additionally, residual TAC within the coating may undergo oxidation-induced volumetric expansion, which also affects porosity. Consequently, these influencing factors contribute to the complex interplay observed in the porosity and density variations of the coatings.

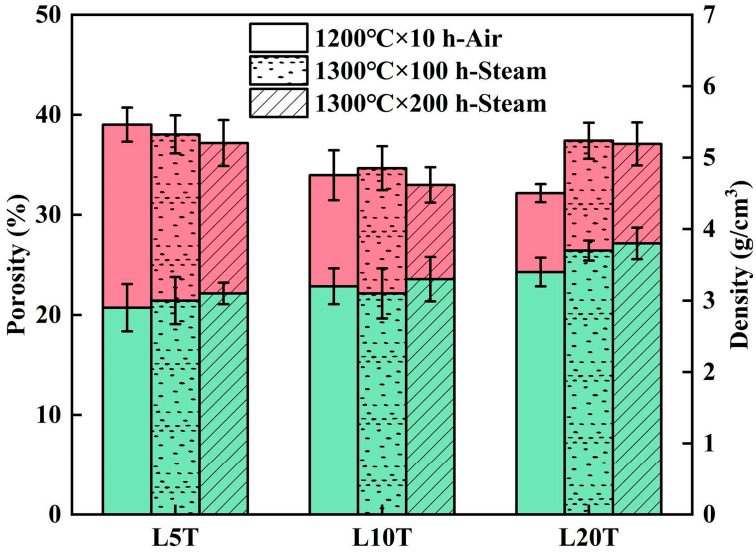

Figure 18. Changes of porosity and density of the composite coatings after annealing at 1200 °C and steam corrosion at 1300 °C. The red bars indicate porosity, and the green bars represent density.

It is noteworthy that the L20T sample exhibited notable phase stability and minimal loss of material in a steam-corrosion environment. Despite increased porosity due to corrosion, the pores remain closed, suggesting a negligible impact on coating lifespan. However, the addition of TAC and the formation of LTA, TiO_2, and Al_2O_3 resulted in increased hardness, which is detrimental to abradability and may lead to increased blade-tip wear. Further work should focus on developing a coating system and applying it to superalloys or even ceramic matrix composites (CMCs) to verify its feasibility. Additionally, the presence of TiO_2 in the coating may improve resistance to CMAS (calcium-magnesium-alumino-silicate) attack—an issue that porous coatings often struggle to mitigate.

4. Conclusions

In this study, LMA-based composite coatings were prepared using the APS process. The effects of TAC as a self-healing agent and sintering aid on the phase composition and microstructure of the composite coatings were thoroughly investigated. Additionally, the air-oxidation and steam-corrosion behaviors at 1300 °C were explored. The main conclusions are as follows:

1. The oxidation of TAC at 1200 °C produced rutile TiO_2 and Al_2O_3, which accelerated sintering, promoted the growth of LMA grains, and reacted with the La-rich secondary phase in the coatings to form LTA. With the increase in TAC content, the coating porosity decreased, and the density increased, converting interconnected pores into isolated ones, while cracks gradually closed.
2. During air oxidation at 1300 °C, the residual TAC in the coatings continued to oxidize, causing a slight weight gain. Excess TiO_2 led to the formation of the $La_4Ti_3O_{12}$ phase. In the composite coatings with higher TAC content, LMA platelet-like grains gradually transformed into equiaxed ones with the oxidation time, and the porosity of the coatings increased.
3. During steam corrosion at 1300 °C, due to the selective volatilization of Al, LTA gradually decomposed to form the α-$La_{2/3}TiO_3$ phase, which further decomposed to produce the $La_4Ti_3O_{12}$ phase. The accelerated mass-transfer effect of steam further increased the thickness of the LMA grains. The steam also caused corrosion within the coatings through the porous structure of the composite coatings. Among them, the composite coating containing 20 wt.% TAC shows the most outstanding stability, indicating its potential as a novel high-temperature abradable material.

Author Contributions: Conceptualization, J.H. and X.C.; methodology, L.D. and J.J.; software, K.L.; formal analysis, S.D.; investigation, M.X.; resources, J.H. and W.C.; data curation, J.H. and M.C.; writing—original draft preparation, J.H.; writing-review and editing, X.C.; supervision, M.C.; project administration, X.C.; funding acquisition, X.C. All authors have read and agreed to the published version of the manuscript.

Funding: This work was financially supported by the National Natural Science Foundation of China (grant numbers U2241238, 52275461, 92060201), the Major Program (JD) of Hubei Province (grant number 2023BAA003), the Key Research and Development Program of Hubei Province (grant number 2023BAB107).

Institutional Review Board Statement: Not applicable.

Informed Consent Statement: Not applicable.

Data Availability Statement: Datasets are available from the corresponding authors upon reasonable request.

Conflicts of Interest: The authors declare no conflicts of interest.

References

1. Sporer, D.; Wilson, S.; Giovannetti, I.; Refke, A.; Giannozzi, M. On The Potential of Metal and Ceramic Based Abradables in Turbine Seal Applications. In Proceedings of the Thirty-Sixth Turbomachinery Symposium, College Station, Texas, USA, 11–13 September 2007; Texas A&M University: College Station, TX, USA, 2007; pp. 79–86. [CrossRef]
2. Bardi, U.; Giolli, C.; Scrivani, A.; Rizzi, G.; Borgioli, F.; Fossati, A.; Partes, K.; Seefeld, T.; Sporer, D.; Refke, A. Development and Investigation on New Composite and Ceramic Coatings as Possible Abradable Seals. *J. Therm. Spray Technol.* **2008**, *17*, 805–811. [CrossRef]
3. Vaßen, R.; Bakan, E.; Mack, D.E.; Guillon, O. A Perspective on Thermally Sprayed Thermal Barrier Coatings: Current Status and Trends. *J. Therm. Spray Technol.* **2022**, *31*, 685–698. [CrossRef]
4. Aussavy, D.; Bolot, R.; Montavon, G.; Peyraut, F.; Szyndelman, G.; Gurt-Santanach, J.; Selezneff, S. YSZ-Polyester Abradable Coatings Manufactured by APS. *J. Therm. Spray Technol.* **2016**, *25*, 252–263. [CrossRef]
5. Sporer, D.R.; Taeck, U.; Dorfman, M.R.; Nicoll, A.R.; Giannozzi, M.; Giovannetti, I. Novel Ceramic Abradable Coatings with Enhanced Performance. In Proceedings of the ASME Turbo Expo 2006: Power for Land, Sea, and Air, Barcelona, Spain, 8–11 May 2006; pp. 1017–1023.
6. Biesiadny, T.J.; Klann, G.A.; Lassow, E.S.; Mchenry, M.; Mcdonald, G.; Hendricks, R.C. Experimental Study of Ceramic-Coated Tip Seals for Turbojet Engines. In Proceedings of the 9th Annual Conference on Composites and Advanced Ceramic Materials: Ceramic Engineering and Science Proceedings, Cocoa Beach, FL, USA, 20–24 January 1985.
7. Cao, X.Q.; Vassen, R.; Stoever, D. Ceramic materials for thermal barrier coatings. *J. Eur. Ceram. Soc.* **2004**, *24*, 1–10. [CrossRef]
8. Sun, J.; Wang, J.; Zhou, X.; Hui, Y.; Dong, S.; Li, L.; Deng, L.; Jiang, J.; Cao, X. Thermal cycling behavior of the plasma-sprayed coating of lanthanum hexaaluminate. *J. Eur. Ceram. Soc.* **2018**, *38*, 1919–1929. [CrossRef]
9. Sun, J.; Wang, J.; Zhang, H.; Yuan, J.; Dong, S.; Jiang, J.; Deng, L.; Zhou, X.; Cao, X. Preparation, structure, mechanical properties and thermal cycling behavior of porous $LaMgAl_{11}O_{19}$ coating. *J. Alloys Compd.* **2018**, *750*, 1007–1016. [CrossRef]
10. Sun, J.; Wang, J.; Zhou, X.; Dong, S.; Deng, L.; Jiang, J.; Cao, X. Microstructure and thermal cycling behavior of plasma-sprayed $LaMgAl_{11}O_{19}$ coatings. *Ceram. Int.* **2018**, *44*, 5572–5580. [CrossRef]
11. Huang, J.; Chen, W.; Lu, X.; Xu, M.; Li, G.; Deng, L.; Jiang, J.; Dong, S.; Liu, L.; Chen, M.; et al. Isothermal Oxidation and Thermal Shock Resistance of Thick and Porous $LaMgAl_{11}O_{19}$ Abradable Topcoat. *Coatings* **2024**, *14*, 426. [CrossRef]
12. Sporer, D.; Wilson, S.; Dorfman, M. Ceramics for Abradable Shroud Seal Applications. *Ceram. Eng. Sci. Proc.* **2009**, *4*, 39–54. [CrossRef]
13. Laverty, W.F. Rub energetics of compressor blade tip seals. *Wear* **1982**, *75*, 1–20. [CrossRef]
14. Sun, J.; Hui, Y.; Jiang, J.; Deng, L.; Cao, X. Crystallization mechanism of plasma-sprayed $LaMgAl_{11}O_{19}$ coating. *Appl. Surf. Sci.* **2020**, *504*, 144509. [CrossRef]
15. Evans, A.G.; Hutchinson, J.W. The mechanics of coating delamination in thermal gradients. *Surf. Coat. Technol.* **2007**, *201*, 7905–7916. [CrossRef]
16. Lee, G.W.; Kim, T.W.; Sloof, W.G.; Lee, K.S. Self-healing capacity of Mullite-Yb_2SiO_5 environmental barrier coating material with embedded Ti_2AlC MAX phase particles. *Ceram. Int.* **2021**, *47*, 22478–22486. [CrossRef]
17. Ando, K.; Chu, M.-C.; Tsuji, K.; Hirasawa, T.; Kobayashi, Y.; Sato, S. Crack healing behaviour and high-temperature strength of mullite/SiC composite ceramics. *J. Eur. Ceram. Soc.* **2002**, *22*, 1313–1319. [CrossRef]
18. Osada, T.; Kamoda, K.; Mitome, M.; Hara, T.; Abe, T.; Tamagawa, Y.; Nakao, W.; Ohmura, T. A Novel Design Approach for Self-Crack-Healing Structural Ceramics with 3D Networks of Healing Activator. *Sci. Rep.* **2017**, *7*, 17853. [CrossRef] [PubMed]
19. Tavangarian, F.; Li, G. Bio-inspired crack self-healing of SiC/spinel nanocomposite. *Ceram. Int.* **2015**, *41*, 2828–2835. [CrossRef]

20. Houjou, K.; Ando, K.; Takahashi, K. Crack-healing behaviour of ZrO_2/SiC composite ceramics. *Int. J. Struct. Integr.* **2010**, *1*, 73–84. [CrossRef]
21. Mohanty, D.; Sil, A.; Maiti, K. Development of input output relationships for self-healing Al_2O_3/SiC ceramic composites with Y_2O_3 additive using design of experiments. *Ceram. Int.* **2011**, *37*, 1985–1992. [CrossRef]
22. Osada, T.; Nakao, W.; Takahashi, K.; Ando, K. Kinetics of Self-Crack-Healing of Alumina/Silicon Carbide Composite Including Oxygen Partial Pressure Effect. *J. Am. Ceram. Soc.* **2009**, *92*, 864–869. [CrossRef]
23. Yuan, M.; Liu, L.; Wang, J.; Hu, Q.; Zhang, H.; Zhang, S.; Zhou, X. Crack-healing behaviour of $MoSi_2$ dispersed $Yb_2Si_2O_7$ environmental barrier coatings. *Ceram. Int.* **2022**, *48*, 29919–29928. [CrossRef]
24. Liu, C.; Cai, C.; Xie, J.; Guo, W.; Qin, H.; Gao, P.; Xiao, H. Effect of surface brittle-to-ductile transition on high-temperature thermal shock resistance of Al_2O_3 ceramics. *Ceram. Int.* **2022**, *48*, 20627–20638. [CrossRef]
25. Yu, H.; Suo, X.; Gong, Y.; Zhu, Y.; Zhou, J.; Li, H.; Eklund, P.; Huang, Q. Ti_3AlC_2 coatings deposited by liquid plasma spraying. *Surf. Coat. Technol.* **2016**, *299*, 123–128. [CrossRef]
26. Wang, X.H.; Li, F.Z.; Chen, J.X.; Zhou, Y.C. Insights into high temperature oxidation of Al_2O_3-forming Ti_3AlC_2. *Corros. Sci.* **2012**, *58*, 95–103. [CrossRef]
27. Tang, C.; Steinbrück, M.; Große, M.; Bergfeldt, T.; Seifert, H.J. Oxidation behavior of Ti_2AlC in the temperature range of 1400 °C–1600 °C in steam. *J. Nucl. Mater.* **2017**, *490*, 130–142. [CrossRef]
28. Lin, Z.J.; Li, M.S.; Wang, J.Y.; Zhou, Y.C. Influence of water vapor on the oxidation behavior of Ti_3AlC_2 and Ti_2AlC. *Scr. Mater.* **2008**, *58*, 29–32. [CrossRef]
29. Yang, H.J.; Pei, Y.T.; Rao, J.C.; De Hosson, J.T.M. Self-healing performance of Ti_2AlC ceramic. *J. Mater. Chem.* **2012**, *22*, 8304–8313. [CrossRef]
30. Song, G.M.; Pei, Y.T.; Sloof, W.G.; Li, S.B.; De Hosson, J.T.M.; van der Zwaag, S. Oxidation-induced crack healing in Ti_3AlC_2 ceramics. *Scr. Mater.* **2008**, *58*, 13–16. [CrossRef]
31. Chen, H.; Hu, B.; Wang, J.; Wang, J.; Gao, Y. Tribological properties of self-healing NiCrAlY/Cr_3C_2-Ti_3AlC_2 coating at high temperatures. *Surf. Coat. Technol.* **2023**, *465*, 129610. [CrossRef]
32. Boatemaa, L.; van der Zwaag, S.; Sloof, W.G. Self-healing of Al_2O_3 containing Ti microparticles. *Ceram. Int.* **2018**, *44*, 11116–11126. [CrossRef]
33. Ma, J.; Hao, J.; Fu, L.; Qiao, Z.; Yang, J.; Liu, W.; Bi, Q. Intrinsic self-lubricity of layered Ti_3AlC_2 under certain vacuum environment. *Wear* **2013**, *297*, 824–828. [CrossRef]
34. Zhao, H.; Feng, Y.; Qian, G.; Huang, X.; Guo, S.; Sun, X. Effect of Ti_3AlC_2 Content on Electrical Friction and Wear Behaviors of Cu–Ti_3AlC_2 Composites. *Tribol. Lett.* **2019**, *67*, 96. [CrossRef]
35. Sun, J.; Wang, J.; Dong, S.; Hui, Y.; Li, L.; Deng, L.; Jiang, J.; Zhou, X.; Cao, X. Effect of heat treatment on microstructure and property of plasma-sprayed lanthanum hexaaluminate coating. *J. Alloys Compd.* **2018**, *739*, 856–865. [CrossRef]
36. Wang, X.H.; Zhou, Y.C. Oxidation behavior of Ti_3AlC_2 powders in flowing air. *J. Mater. Chem.* **2002**, *12*, 2781–2785. [CrossRef]
37. Zhao, K.; Dong, S.; Lü, K.; Chen, T.; Huang, Y.; Hu, Q.; Jiang, J.; Deng, L.; Cao, X. Feasibility research of $Yb_3Al_5O_{12}$ garnet as environmental barrier coating materials. *Ceram. Int.* **2023**, *49*, 15413–15421. [CrossRef]
38. Li, G.; Qin, L.; Cao, X.; Lu, X.; Tu, Y.; Zhang, H.; Jiang, J.; Deng, L.; Dong, S.; Liu, L.; et al. Water vapor corrosion resistance and failure mechanism of SiCf/SiC composites completely coated with plasma sprayed tri-layer EBCs. *Ceram. Int.* **2022**, *48*, 7082–7092. [CrossRef]
39. Qian, X.K.; He, X.D.; Li, Y.B.; Sun, Y.; Li, H.; Xu, D.L. Cyclic oxidation of Ti_3AlC_2 at 1000–1300 °C in air. *Corros. Sci.* **2011**, *53*, 290–295. [CrossRef]
40. Song, G.M.; Pei, Y.T.; Sloof, W.G.; Li, S.B.; De Hosson, J.T.M.; van der Zwaag, S. Early stages of oxidation of Ti_3AlC_2 ceramics. *Mater. Chem. Phys.* **2008**, *112*, 762–768. [CrossRef]
41. Hu, Q.; Liu, R.; Guo, X.; Wei, H.; Tu, Y.; Wang, Y.; Song, G.; Lu, X.; Huang, J.; Xu, M.; et al. Thermal cycling behavior of Si/Yb_2SiO_5/$LaMgAl_{11}O_{19}$ TEBCs coated SiCf/SiC composites under burner rig tests. *Ceram. Int.* **2022**, *48*, 28082–28091. [CrossRef]
42. Chen, X.; Sun, Y.; Hu, J.; Li, J.; Deng, C.; Wu, D.; Zeng, D.; Li, W.; Liu, Y.; Zou, B.; et al. Thermal cycling failure of the multilayer thermal barrier coatings based on $LaMgAl_{11}O_{19}$/YSZ. *J. Eur. Ceram. Soc.* **2020**, *40*, 1424–1432. [CrossRef]
43. Chen, X.; Zhao, Y.; Huang, W.; Ma, H.; Zou, B.; Wang, Y.; Cao, X. Thermal aging behavior of plasma sprayed $LaMgAl_{11}O_{19}$ thermal barrier coating. *J. Eur. Ceram. Soc.* **2011**, *31*, 2285–2294. [CrossRef]
44. Naghizadeh, R.; Rezaie, H.R.; Golestani-Fard, F. Effect of TiO_2 on phase evolution and microstructure of $MgAl_2O_4$ spinel in different atmospheres. *Ceram. Int.* **2011**, *37*, 349–354. [CrossRef]
45. Xu, L.; Chen, M.; Yin, X.-l.; Wang, N.; Liu, L. Effect of TiO_2 addition on the sintering densification and mechanical properties of $MgAl_2O_4$–$CaAl_4O_7$–$CaAl_{12}O_{19}$ composite. *Ceram. Int.* **2016**, *42*, 9844–9850. [CrossRef]
46. Lu, X.; Yuan, J.; Li, G.; Xu, M.; Lu, G.; Zhang, Y.; Yuan, F.; Huang, J.; Deng, L.; Jiang, J.; et al. Preparation and properties evaluation of high-entropy $(La_{0.2}Nd_{0.2}Sm_{0.2}Eu_{0.2}Gd_{0.2})MgAl_{11}O_{19}$ for advanced thermal barrier coating. *J. Eur. Ceram. Soc.* **2024**, *44*, 6641–6650. [CrossRef]
47. Lv, B.; Fan, X.; Xie, H.; Wang, T.J. Effect of neck formation on the sintering of air-plasma-sprayed thermal barrier coating system. *J. Eur. Ceram. Soc.* **2017**, *37*, 811–821. [CrossRef]

48. Hao, W. Study on the Preparation and Thermo-Physical Properties of Modified Lanthanum–Titanium–Aluminu Oxide Thermal Barrier Coatings. Master's Thesis, Beihang University, Bejing, China, 2013. (In Chinese)
49. Li, X.; Qian, Y.; Zheng, L.; Xu, J.; Li, M. Determination of the critical content of Al for selective oxidation of Ti_3AlC_2 at 1100 °C. *J. Eur. Ceram. Soc.* **2016**, *36*, 3311–3318. [CrossRef]
50. Li, X.; Zheng, L.; Qian, Y.; Xu, J.; Li, M. Breakaway oxidation of Ti_3AlC_2 during long-term exposure in air at 1100 °C. *Corros. Sci.* **2016**, *104*, 112–122. [CrossRef]
51. Lozano-Mandujano, D.; Poblano-Salas, C.A.; Ruiz-Luna, H.; Esparza-Esparza, B.; Giraldo-Betancur, A.L.; Alvarado-Orozco, J.M.; Trápaga-Martínez, L.G.; Muñoz-Saldaña, J. Thermal Spray Deposition, Phase Stability and Mechanical Properties of $La_2Zr_2O_7/LaAlO_3$ Coatings. *J. Therm. Spray Technol.* **2017**, *26*, 1198–1206. [CrossRef]
52. Škapin, S.; Kolar, D.; Suvorov, D. X-ray Diffraction and Microstructural Investigation of the Al_2O_3-La_2O_3-TiO_2 System. *J. Am. Ceram. Soc.* **1993**, *76*, 2359–2362. [CrossRef]
53. Zhang, Q.; McGinn, P.J. Microstructure and Dielectric Properties of a $LaAlO_3$–TiO_2 Diffusion Couple. *J. Am. Ceram. Soc.* **2006**, *89*, 1687–1693. [CrossRef]
54. Xie, X.; Guo, H.; Gong, S.; Xu, H. Thermal cycling behavior and failure mechanism of $LaTi_2Al_9O_{19}$/YSZ thermal barrier coatings exposed to gas flame. *Surf. Coat. Technol.* **2011**, *205*, 4291–4298. [CrossRef]
55. Wada, M.; Matsudaira, T.; Kawashima, N.; Takeuchi, M.; Yokoe, D.; Ogawa, T.; Kato, T.; Takata, M.; Kitaoka, S. Effect of Water Vapor on Mass Transfer in Polycrystalline $Yb_2Si_2O_7$ under Oxygen Potential Gradients at High Temperatures. *Acta Mater.* **2020**, *201*, 373–385. [CrossRef]
56. Chen, X.; Zhang, Y.; Zhong, X.; Xu, Z.; Zhang, J.; Cheng, Y.; Zhao, Y.; Liu, Y.; Fan, X.; Wang, Y.; et al. Thermal cycling behaviors of the plasma sprayed thermal barrier coatings of hexaluminates with magnetoplumbite structure. *J. Eur. Ceram. Soc.* **2010**, *30*, 1649–1657. [CrossRef]
57. Bakan, E.; Sohn, Y.J.; Kunz, W.; Klemm, H.; Vassen, R. Effect of processing on high-velocity water vapor recession behavior of Yb-silicate environmental barrier coatings. *J. Eur. Ceram. Soc.* **2019**, *39*, 1507–1513. [CrossRef]
58. Richards, B.T.; Young, K.A.; de Francqueville, F.; Sehr, S.; Begley, M.R.; Wadley, H.N.G. Response of ytterbium disilicate-silicon environmental barrier coatings to thermal cycling in water vapor. *Acta Mater.* **2016**, *106*, 1–14. [CrossRef]
59. Gadow, R.; Schaefer, G. Thermal Insulating Material and Method of Producing Same. U.S. Patent US6998064B2, 14 February 2006.

Disclaimer/Publisher's Note: The statements, opinions and data contained in all publications are solely those of the individual author(s) and contributor(s) and not of MDPI and/or the editor(s). MDPI and/or the editor(s) disclaim responsibility for any injury to people or property resulting from any ideas, methods, instructions or products referred to in the content.